Proton and Oxide Ion Conductivity in Palmierite Oxides

Sacha Fop,[1,2,*] James A. Dawson,[3,4] Dylan N. Tawse,[2] Matthew G. Skellern,[2] Jan M. S. Skakle,[2] and Abbie C. Mclaughlin[2]

[1] ISIS Facility, Rutherford Appleton Laboratory, Harwell OX11 0QX, United Kingdom

[2] The Chemistry Department, University of Aberdeen, Aberdeen AB24 3UE, United Kingdom

[3] Chemistry – School of Natural and Environmental Science, Newcastle University, Newcastle NE1 7RU, United Kingdom

[4] Centre for Energy, Newcastle University, Newcastle NE1 7RU, United Kingdom

ABSTRACT: Solid proton and oxide ion conductors have key applications in several hydrogen-based and energy related technologies. Here we report on the discovery of significant proton and oxide ion conductivity in palmierite oxides $A_3V_2O_8$ (A = Sr, Ba), which crystallize with a framework of isolated tetrahedral VO_4 units. We show that these systems present prevalent ionic conduction, with a large protonic component under humidified air ($t_H \sim 0.6 – 0.8$) and high protonic mobility. In particular, the proton conductivity of $Sr_3V_2O_8$ is 1.0 x 10^{-4} S cm^{-1} at 600 °C, competitive with the best proton conductors constituted by isolated tetrahedral units. Simulations show that the three-dimensional ionic transport is vacancy driven and is facilitated by rotational motion of the VO_4 units, which can stabilize oxygen defects via formation of V_2O_7 dimers. Our findings demonstrate that palmierite oxides are a new promising class of ionic conductors where stabilization of parallel vacancy and interstitial defects can enable high ionic conductivity.

Introduction

Solid proton and oxide ion conductors are important materials with applications in a range of hydrogen-based electrochemical energy technologies, from ceramic fuel cells (CFCs) to electrolyzers (SOECs) and chemical reactors. [1, 2, 3, 4, 5, 6, 7, 8, 9] To make these technologies more economical and durable, it is important to develop ionic conductors with high conductivities at reduced temperatures (≤ 600 °C). Ionic conduction strongly depends on the characteristics of the crystal structure, and the discovery of new solid proton and oxide ion conductors crucially depends on exploring novel structure types and materials.

Several oxide ion and proton conductors crystallize with the perovskite ABO_3 structure, which is composed by a three-dimensional network of corner-sharing BO_6 octahedra. [10, 11, 12, 13, 14] In these perovskite-type materials, the defects necessary for ionic transport are usually created with the insertion of extrinsic oxygen vacancies by acceptor doping. [10, 14, 15] The oxygen vacancies can enable oxide ion diffusion and provide sites for the dissociative absorption of water and creation of protonic defects. Oxide ion migration in perovskite-type oxides occurs via vacancy hopping between oxygen sites along a BO_6 octahedron edge, [15, 16] whereas proton transport generally follows a Grotthuss mechanism characterized by the fast rotational diffusion of the protonic defect around an oxygen atom, followed by intra-octahedral hopping towards a neighboring oxide ion. [10, 17] Proton and oxide ion diffusion along frameworks of corner-sharing octahedral units is a common feature of several ionically conducting oxides. [18, 19, 20] Reports of significant proton or oxide ion transport in oxide structures constituted by isolated tetrahedral units are on the other hand relatively scarce. Examples comprise proton conduction in acceptor-doped scheelite- and monazite-type oxides $LaMO_4$ (M = P, V, As, Nb, Sb, Ta) [21, 22, 23, 24, 25, 26], lanthanum-barium gallates of general formula $La_{1-x}Ba_{1+x}GaO_{4-x/2}$,[27, 28] and acceptor-doped Gd_3GaO_6.[29] Similarly, oxide ion conduction has been reported only in a few structural families constituted by isolated tetrahedral units, namely apatites and scheelites. [30, 31, 32]

We have recently reported proton and oxide ion conduction in a series of cation deficient hexagonal perovskite derivatives formed by a disordered combination of perovskite and palmierite-like layers [33, 34, 35, 36, 37, 38, 39, 40]. The latter are composed by isolated tetrahedral units which have a particular topology that allows water incorporation and fast ionic transport. This is demonstrated by the high proton and oxide ion conductivity exhibited by the hexagonal perovskite derivative $Ba_7Nb_4MoO_{20}$ (respectively 4.0 x 10^{-3} S cm^{-1} and 2.0 x 10^{-3} S cm^{-1} at 500 °C), and the high oxide ion conductivity of $Ba_3Nb_{0.9}V_{0.1}MoO_{8.5}$ (1.0 x 10^{-2} S cm^{-1} at 600 °C), both comparable to state-of-the-art doped perovskite-type ionic conductors. [39, 40] On the basis of such findings, we have investigated the ionic conductivity of palmierite oxides with composition $A_3V_2O_8$ (A = Sr, Ba). The palmierite structure is a cation-deficient derivative of the 9R hexagonal perovskite polytype $A_3B_2O_9$, where the

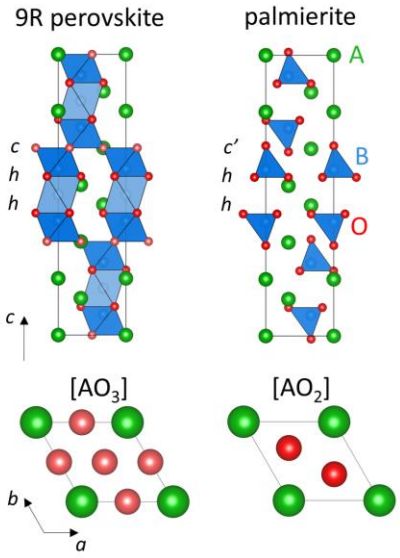

Figure 1. Comparison between the 9R hexagonal perovskite and palmierite structures. The palmierite s tructure is a cation deficient derivative of the 9R perovskite where the cubic [AO_3] layer of the stacking sequence $(hhc)_3$ is replaced by an oxygen deficient [AO_2] layer (c'). Crystallographically, the palmierite structure can be obtained from the 9R perovskite by shifting of the oxygen atom on Wyckoff position 9*e* (½,0,0) to 6*c* (0,0,~ ⅓). Note how the central octahedron of the metal trimers is unoccupied in the palmierite structure.

cubic [AO_3] layer of the stacking sequence $(hhc)_3$ is replaced by a layer of composition [AO_2], thus generating layers of isolated tetrahedral units spaced by empty octahedral sites (Figure 1). [41, 42] Here, we report on the discovery of significant proton and oxide ion conductivity in $A_3V_2O_8$ for the first time, thus demonstrating that palmierite oxides with isolated tetrahedral units can constitute a new family of ionic conductors.

Experimental section

Synthesis and characterization. Samples of $A_3V_2O_8$ (with A = Sr, Ba) were synthesized by solid-state reaction method. Stoichiometric amounts of $SrCO_3$ (99.995%, Aldrich) or $BaCO_3$ (99.999%, Aldrich) and V_2O_5 (99.95%, Aldrich) were ground, pressed into a pellet, heated at 1100 °C for 10h and then cooled to room temperature at 5 °C/min. The heating step was repeated a second time to obtain a phase pure product. Sample purity was confirmed by laboratory X-ray diffraction (XRD), using a PANalytical Empyrean diffractometer equipped with a Cu Ka tube and a Johansson monochromator. Data were recorded in the range 10° < 2θ < 120° with a step size of 0.013°. Thermogravimetric analysis (TGA) was performed with a Mettler Toledo TGA 2 on samples stored at ambient conditions. The samples were heated at 200 °C for 10 h prior the analysis in order to remove any adsorbed surface water.

Impedance spectroscopy. The electrical properties of $A_3V_2O_8$ (with A = Sr, Ba) were measured by AC impedance spectroscopy, with a Solartron 1260 impedance analyzer in the frequency range 0.1 Hz – 1 MHz with an applied alternating voltage of 0.1 V. Measurements were performed on platinum coated dense pellets (~ 90% of the theoretical neutron diffraction density) of approximately ~ 1 mm thickness and ~10 mm diameter, upon cooling from 800 °C in a sealed tube furnace and allowing 2 hours of equilibration at each temperature step. Dry gaseous atmospheres, obtained by flowing the employed gas through a column of a commercial desiccant (Drierite) ($pH_2O < 10^{-4}$ atm), were employed for the measurements in air, O_2, N_2 and 5% H_2/N_2. For the measurements in humidified air, the gas was bubbled through a water-filled Dreschel bottle at ambient temperature (pH_2O ~ 0.021 atm). Total resistivity values (R_b + R_{gb}) were extracted from the high frequency intercept of the arcs on the real impedance axis. In addition, equivalent circuit analysis was used to extract the individual bulk and grain boundary responses for $Sr_3V_2O_8$; a detailed description of the analysis can be found in the Supporting Information.

Neutron diffraction and structural analysis. Room temperature high resolution neutron diffraction experiments were performed on the time-of-flight (TOF) High Resolution Powder Diffractometer (HRPD) at ISIS (Rutherford Appleton Laboratory, Harwell, Oxford, UK). 5 g of $A_3V_2O_8$ (A = Sr, Ba) powder samples were loaded into a vanadium can and measured at room temperature (25 °C) with total scan time of 4 hours.

Rietveld analysis was performed using the GSAS/EXPGUI package. [43] The palmierite structure reported in ref. 42 was employed as the initial model for the Rietveld refinements. The metal A cations are on two different positions, A1 (at Wyckoff site 3*a*) and A2 (at Wyckoff site 6*c*), while the vanadium atom occupy a single position (at Wyckoff site 6*c*). The oxygen atoms are on two positions, O1 at Wyckoff site 6*c* and O2 at Wyckoff site 18*h*. Data from both the high-resolution back-scattering detector bank and the 90° detector bank were employed for the structural refinements of the measurements collected on HRPD. The background was fitted with the Chebyshev polynomial function and peak shapes were modelled using a pseudo-Voigt function.

Bond-valence site energy (BVSE) calculations were performed with the *softB*V program, [44, 45] using the structural models from Rietveld refinement as input. Bond-valence site energy landscapes for the interaction of test H^+ and O^{2-} ions were calculated for a dense grid of points with a resolution of 0.1 Å. Energy minimum equilibrium sites and diffusion pathways were identified with regions of low bond-valence site energy by direct visualization of the isosurfaces and by examination of the calculated energy profiles.

Computational methods. Density functional theory simulations were carried out with the Vienna ab initio simulation package (VASP). A plane-wave cutoff energy of 520 eV and a k-point mesh spacing smaller than 0.05 $Å^{-1}$ were utilized for the geometry optimization calculations. The projector augmented wave method [46] and the PBEsol exchange-correlation functional [47] were employed for all calculations. Single unit cells and 2×2×1 supercells of

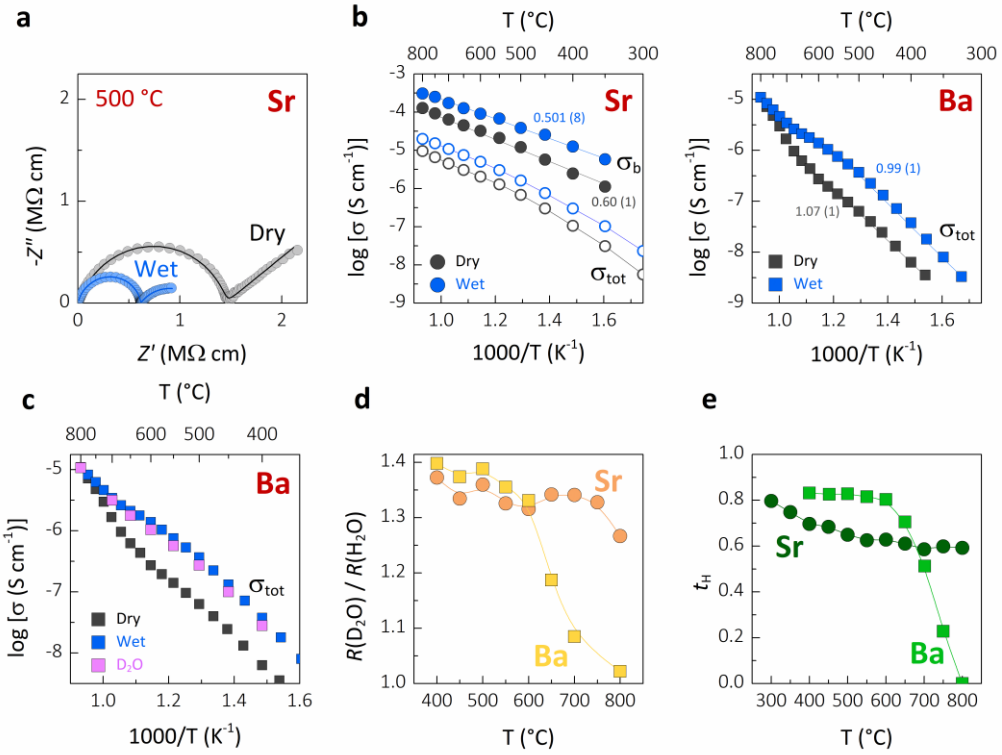

Figure 2. (a) Typical complex impedance plots for $Sr_3V_2O_8$ collected under dry and humidified air. The line represents the equivalent circuit fitting to the data. **(b)** Arrhenius plots of the bulk and total conductivity of $Sr_3V_2O_8$ and the total conductivity of $Ba_3V_2O_8$ collected under dry and humidified air atmospheres with the respective activation energies (in eV). **(c)** Arrhenius plot showing a reduction of the total conductivity of $Ba_3V_2O_8$ under air + D_2O atmosphere due to the isotope effect. **(d)** Plot of the resistivity ratio of the sample in air + D_2O and air + H_2O. **(e)** Calculated proton transport number.

$Ba_3V_2O_8$ and $Sr_3V_2O_8$ were used to calculate the hydration energetics, with the number of water molecules (nH_2O) per formula unit equal to 0 (dehydrated), 0.0825 or 0.330. The unit cell parameters for the computed structures are reported in Table S1. Ab initio molecular dynamics (AIMD) simulations were utilized with a plane-wave cutoff energy of 400 eV and the k-space was sampled using the gamma-point only. To investigate proton transport, AIMD runs of 50 ps at 800, 1000 and 1200 K using the NVT ensemble with the Nose−Hoover thermostat [48] were used in 2×2×1 $A_3V_2O_8 \cdot 0.0825H_2O$ and $A_3V_2O_8 \cdot 0.330H_2O$ (A = Sr, Ba) supercells containing 168 and 159 ions, respectively. A time step of 1 fs was used to account for the motion of the protons. To determine the oxide ion transport mechanism, 30-ps AIMD simulations of $Sr_3V_2O_8$ with and without oxygen vacancies at 1200 K were carried out using a 2×2×1 supercell and a time step of 2 fs.

Results and discussion

Ionic conductivity. $A_3V_2O_8$ samples were synthesized via solid-state reaction at 1100 °C. The purity of the as prepared phases was confirmed by laboratory X-ray diffraction (Figure S1). AC impedance spectroscopy measurements under variable atmospheres were employed to investigate the ionic conductivity of $A_3V_2O_8$. Typical complex impedance Z^* plots recorded in dry ($pH_2O < 10^{-4}$ atm) and humidified ($pH_2O \sim 0.021$ atm) air are shown in Figure 2a and Figure S2. The plots for $Sr_3V_2O_8$ show a broad and depressed grain arc constituted by the overlap of the bulk (~ 6.2 – 8.3 pF cm^{-1}) and grain boundary (~ 0.01 – 0.02 nF cm^{-1}) responses, which are clearly identifiable in the high and intermediate frequency regions of the complex modulus (M^*) plots (Figure S3a, b) [49]. The data of $Ba_3V_2O_8$ show a single signal which can be associated to the overall grain response (~ 4.7 – 6.5 pF cm^{-1}) (Figure S3c, d). The complex impedance plots display a clear reduction in resistivity on going from dry to humidified air. The Arrhenius plots in Figure 2b show a marked increase in conductivity, indicating proton conduction. The bulk conductivity of $Sr_3V_2O_8$ in humidified air (1.0 x 10^{-4} S cm^{-1} at 600 °C) is higher than the bulk conductivity measured in dry air (3.2 x 10^{-5} S cm^{-1}). The conductivity of $Ba_3V_2O_8$ shows an increase of nearly one order of magnitude in humidified air, from 1.8 x 10^{-7} S cm^{-1} to 1.6 x 10^{-6} S cm^{-1} at 600 °C. The presence of proton conduction is further corroborated by impedance spectroscopy measurements in air + D_2O, which clearly show a reduction in conductivity due to the isotope effect (Figure 2c and Figure S6). The ratio between the resistivity values measured in air + D_2O and air + H_2O is ~ 1.3 – 1.4 (Figure 2d), approaching the expected theoretical value of $\sqrt{2}$ [50]. The proton transport number, t_H, calculated from the total conductivity values in dry and humidified air atmospheres, [51] is in the range ~ 0.6 – 0.8 for $Sr_3V_2O_8$ and ~ 0.82 below 600 °C for $Ba_3V_2O_8$, demonstrating significant proton conductivity (Figure 2e).

A low-slope electrode signal is observed at low frequencies both in dry and humidified atmospheres (Figure 2a and Figure S4) and indicates finite length diffusion typical of a Warburg electrode response. This feature is diagnostic of ionic conduction in a material with partially blocking electrodes [49]. The presence of a prominent Warburg spike in dry air atmosphere (Figure 2a and Figure S4) would indicate oxide ion conduction. Further measurements under a range of dry atmospheres (air, O_2, N_2, 5% H_2 in N_2) show that the total conductivity is independent of oxygen partial pressure at high and intermediate pO_2 values (Figure S7), demonstrating that $A_3V_2O_8$ presents predominantly oxide ion conductivity. There is an increase in conductivity in 5% H_2 in N_2 atmosphere, suggesting an electronic *n*-type component. However, the presence of clear Warburg/electrode responses (Figure S7a), which would have been absent in the case of largely electronic transport, at all temperatures in the Z^* plots recorded under the more reducing conditions indicates that the electronic component is small and that the conductivity is predominantly ionic. [52]

These results demonstrate for the first time that $A_3V_2O_8$ presents significant proton and oxide ion conduction, with the A = Sr sample showing the highest conductivity. In particular, the bulk proton conductivity of palmierite $Sr_3V_2O_8$ is competitive with the conductivities of acceptor doped $La_{0.99}Ca_{0.01}MO_4$ (M = Nb, Ta) [22, 23] and $La_{0.8}Ba_{1.2}GaO_{3.9}$ [27], which are among the best proton conductors constituted by isolated tetrahedral units. The conductivity of $Sr_3V_2O_8$ is also considerably higher than the proton conductivities of the oxygen deficient perovskite derivative $Ba_3YGa_2O_{7.5}$ [53] and of doped langasite $La_3Ga_5SiO_{14}$ [54], both containing tetrahedral units with only three of their four corners connected to other framework polyhedra, and of cuspidine $La_4Ga_2O_9$-based oxides [55], which are formed by corner sharing tetrahedral units (Figure 3). $A_3V_2O_8$ palmierite oxides are currently undoped so that targeted chemical doping should further enhance the proton and oxide ion conductivity.

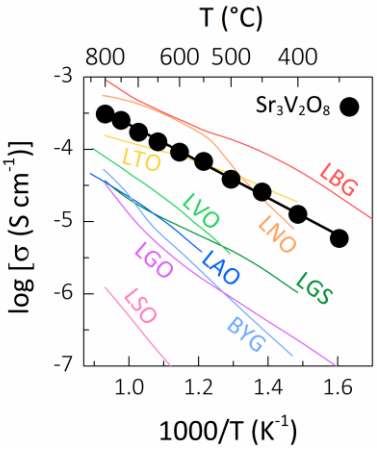

Figure 3. Arrhenius plot of the bulk proton conductivity of $Sr_3V_2O_8$ in humidified air compared with the proton conductivities of $La_{0.8}Ba_{1.2}GaO_{3.9}$ (LBG) [27], $La_{0.99}Ca_{0.01}NbO_4$ (LNO) [22], $La_{0.99}Ca_{0.01}TaO_4$ (LTO) [23], $La_{0.99}Ca_{0.01}VO_4$ (LVO) [24], $La_{0.99}Sr_{0.01}AsO_4$ (LAO) [25], $La_{0.99}Ca_{0.01}SbO_4$ (LSO) [26], $Ba_3YGa_2O_{7.5}$ (BYG) [53], $La_3Ga_{5.06}Si_{0.94}O_{14}$ (LGS) [54], $La_4GaTiO_{9.5}$ (LGO) [55].

Crystal structure. The structures of $A_3V_2O_8$ (A = Sr, Ba) were investigated by Rietveld refinement employing the previously reported model [42]. Preliminary refinement of the crystal structures from high resolution X-ray diffraction (see Figure S8 and Table S2) showed that $A_3V_2O_8$ crystallizes with the palmierite structure (space group $R\bar{3}m$) which is composed by layers of isolated VO_4 tetrahedral units spaced by empty cationic vacancies. X-ray difference Fourier maps confirmed that V occupies only the 6*c* Wyckoff site and that the vacancies are ordered (Figure S9), in contrast with what seen in some hybrid hexagonal perovskite-palmierite $Ba_3M'M''O_{8.5}$ (*M*' = Nb; *M*" = Mo, W) materials, where the cation vacancies are disordered [38, 39, 56, 57]. Previous neutron diffraction studies have shown that materials reported to have the palmierite structure can have more complex oxygen ordering leading to the formation of hexagonal polytype structures with face- or corner-sharing octahedral units, e.g. $Ba_3Nb_2O_8$ [58]. For this reason, neutron diffraction, which is more sensitive to the oxygen sub-lattice, was performed on the High Resolution Powder Diffractometer (HRPD) at the ISIS Neutron and Muon Source at room temperature [59]. Refinement of the crystal structures from neutron diffraction data resulted in an excellent fit to the data (see Figure S10 and Table S3), thus confirming that $A_3V_2O_8$ (A = Sr, Ba) indeed crystallise in the palmierite structure with layers of isolated tetrahedral units (Figure 4a, b).

To investigate the possible proton positions, the energy landscape for a test H^+ was calculated by the bond-valence sum (BVS) method with the software *soft*BV [44, 45], using the structural models from Rietveld refinement as input. The lowest energy (0.0 eV, absolute BVSE minimum) proton site H1 was identified around the apical tetrahedral oxygen O1, at Wyckoff position 18*h* (~ 0.11, ~ 0.22, ~ 0.32) (Figure 3b). This was also confirmed by DFT calculations for both $Sr_3V_2O_8$ and $Ba_3V_2O_8$, with protons either occupying Wyckoff position 18*h* or a site between adjacent oxide ions that acts as a transition state for proton migration. The O1–H1 bond length is ~ 1.09 Å and ~1.02 Å from BVS calculations and DFT simulations, respectively, in agreement with values determined in other proton conductors [60, 61].

Ionic conduction mechanism. AIMD simulations at a range of temperatures (800, 1000 and 1200 K) on two different hydrated compositions ($A_3V_2O_8{\cdot}0.0825H_2O$ and $A_3V_2O_8{\cdot}0.330H_2O$), were used to further investigate the level and mechanism of proton conduction in these palmierite materials. The AIMD trajectory plot for protons in $Sr_3V_2O_8{\cdot}0.0825H_2O$ at 1200 K in Figure 5a shows a three-dimensional percolation network, with long-range proton rotation and hopping primarily along the *ab* plane. Proton hopping occurs across the O1 anions and also from O1 to O2, but the protons can become trapped by the intrinsic cationic vacancies. BVSE calculations for the interaction of a probe H^+ ion confirmed the lowest-energy 2-dimensional proton conduction pathway, with proton exchange between the H1 positions (BVSE barrier ~ 0.20 eV) and

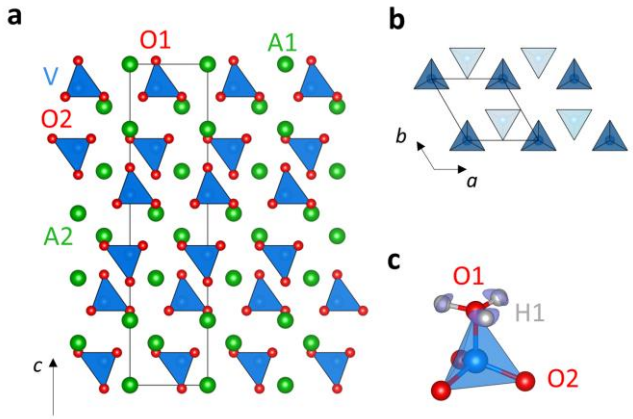

Figure 4. (a) Crystal structure of $A_3V_2O_8$ (A = Sr, Ba). **(b)** Distribution of the VO_4 units within two adjacent tetrahedral layers as seen along the [001] direction. **(c)** Proton equilibrium position in relation to the VO_4 tetrahedron as obtained by BVSE and DFT calculations. BVSE isosurface levels are at 0.0 eV.

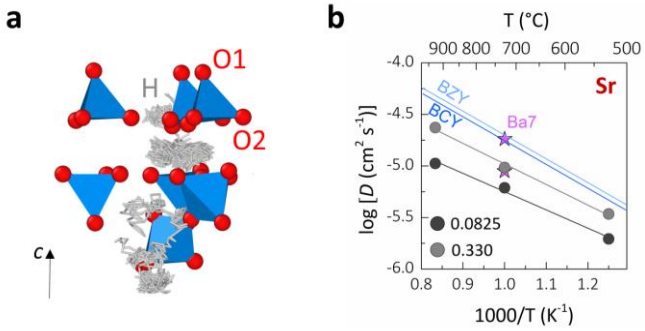

Figure 5. (a) AIMD trajectory plot for protons in $Sr_3V_2O_8{\cdot}0.0825H_2O$ at 1200 K. **(b)** Arrhenius plot of the calculated proton diffusion coefficient for $Sr_3V_2O_8{\cdot}nH_2O$, with n = 0.0825 and 0.330. The diffusion coefficients for perovskite-type proton conductors $BaCe_{0.98}Y_{0.02}O_{3-\delta}$ (BCY) and $BaZr_{0.9}Y_{0.2}O_{3-\delta}$ (BZY) [62] and for $Ba_7Nb_4MoO_{20}{\cdot}nH_2O$ with n = 0.125 and 0.5 (Ba7) [63] are also plotted for comparison.

hopping onto an adjacent O1 atom (BVSE barrier ~ 0.20 – 0.23 eV) (Figure S11). While the 2D proton conduction pathway dominates in both $Sr_3V_2O_8{\cdot}0.0825H_2O$ and $Ba_3V_2O_8{\cdot}0.0825H_2O$, the AIMD simulations for the materials with a higher water content ($A_3V_2O_8{\cdot}0.330H_2O$) show a transition towards a more isotropic 3D hopping mechanism. To quantify the levels of proton transport in these materials, we calculated the mean squared displacements of the protons and used them to derive proton diffusion coefficients. The calculated diffusion coefficients are presented through Arrhenius plots in Figure 5b and Figure S12. We obtained proton diffusion coefficients of 1.96×10^{-6} and 3.42×10^{-6} $cm^2\ s^{-1}$ at 800 K for $Sr_3V_2O_8{\cdot}0.0825H_2O$ and $Sr_3V_2O_8{\cdot}0.330H_2O$, respectively. In agreement with our conductivity analysis, lower values of 7.89×10^{-7} and 1.47×10^{-6} $cm^2\ s^{-1}$ at 800 K were found for $Ba_3V_2O_8{\cdot}0.0825H_2O$ and $Ba_3V_2O_8{\cdot}0.330H_2O$, respectively. These values are comparable with other high-performance proton conductors [10, 62] and the hexagonal perovskite derivative $Ba_7Nb_4MoO_{20}$, [63] which also contains palmierite-like layers, thus confirming the high mobility of the protonic defects in the $A_3V_2O_8$ structure.

The observed enhancement in proton diffusion as a result of increased hydration in these materials may represent a potential route to their increased conductivity. However, this is reliant on achieving high proton concentrations in the materials experimentally, possibly through acceptor doping strategies. Thermogravimetric analysis (TGA) demonstrate that $A_3V_2O_8{\cdot}nH_2O$ samples stored at ambient conditions have water concentrations of n = 0.008 for A = Sr and n = 0.013 for Ba (Figure S13), considerably lower than the value of ~ 0.80 H_2O molecules per formula unit found for $Ba_7Nb_4MoO_{20}$. [40, 63] The low concentrations of water measured in the samples are commensurate with our DFT calculations that predict endothermic hydration enthalpies in the range 10.61 to 87.80 kJ mol^{-1} (Table S5).

These large positive values illustrate the weak hygroscopicity of the materials, particularly when compared to the typically strong exothermic values found for other well-known solid-state proton conductors, including those with palmierite-like layers, such as $Ba_7Nb_4MoO_{20}$ [63]. In our previous study of $Ba_7Nb_4MoO_{20}$ we found that water is absorbed on the intrinsic oxygen vacancies present on the palmierite-like layer, and that hydration is linked to a shift from the tetrahedral NbO_4 and MoO_4 units in the palmierite-like layer to the equivalent NbO_6 and MoO_6 octahedra by filling of the adjacent cation vacancy, resulting in a strong increase in the exothermic hydration enthalpies. [63] DFT geometry optimization calculations on $A_3V_2O_8$ with a VO_4 unit changed to a VO_6 unit as well as with a proton located in a close vicinity to a vanadium ion in an attempt to "push" it from the tetrahedral to octahedral coordination demonstrate that this phenomenon does not occur on these palmierite oxides. This fundamental difference in the behavior between $A_3V_2O_8$ and $Ba_7Nb_4MoO_{20}$ helps to explain why hydration of the former is severely limited. The hexagonal derivative $Ba_3VWO_{8.5}$, which is constituted by layers of isolated V/W polyhedral units spaced by ordered cationic vacancies analogous to the palmierite structure, similarly does not exhibit significant water absorption because of the strong preference of V^{5+} for tetrahedral geometry [64]. It is likely that the as-prepared $A_3V_2O_8$ materials present a small oxygen non stoichiometry (not visible by neutron diffraction and generated by heating or the high temperature synthesis) which enables low concentrations of water absorption. To confirm this, we considered the possibility of water molecules absorbing at pre-existing oxygen vacancy sites by comparing the energetics of the materials with an oxygen vacancy with those of the hydrated ($0.0825H_2O$) phases. This resulted in exothermic hydration enthalpies of -63.00 and -32.81 kJ mol^{-1} for $Sr_3V_2O_8$ and $Ba_3V_2O_8$, respectively, suggesting that the hydration of these materials can become favorable when they are sufficiently oxygen deficient.

AIMD simulations were also used to determine the mechanism of oxide ion transport in these materials. We considered two models of $Sr_3V_2O_8$, i.e., with and without oxygen vacancies. In the pristine system without defects, no long-range ion diffusion or VO_4 rotational disorder is observed. In contrast, in the system with an oxygen vacancy concentration of 6.25%, both long-range ion diffusion and VO_4 rotational disorder are found, and our simulations reveal that they are unequivocally linked. As shown in Figure 6a, oxide ion transport in these materials is vacancy driven and occurs via the formation of V_2O_7 groups, where an oxygen atom from a VO_4 group transitions to the vacant site of an oxygen-deficient VO_3 group. Given the relatively large interatomic distances between the V ions in $Sr_3V_2O_8$ and $Ba_3V_2O_8$ (> 3.76 and 3.95 Å, respectively), the rotation of VO_4 groups is pivotal in facilitating ion transport in these materials. Such mechanism of oxygen migration via the synergic rotation and deformation of VO_4 units to allow the breaking and reforming of V_2O_7 dimers is analogous to the one reported in $La_{1-x}Ba_{1+x}GaO_{4-x/2}$ and scheelite $Bi_{1-x}Sr_xVO_{4-0.5x}$, both formed by isolated tetrahedral moieties. [28, 31] It is likely that the high dynamical and rotational flexibility of the isolated tetrahedral moieties also assist the proton transport, in analogy with the case of $Ba_7Nb_4MoO_{20}$ and the solid-acid protonic conductor CsH_2PO_4. [63, 65] The AIMD simulations show a three-dimensional oxide-ion diffusion pathway, with exchange between O1–O1, O1–O2 and O2–O2 positions (see circled areas in Figure 6b). This is in contrast with the two-dimensional oxide ion diffusion pathway along the *ab* plane reported for hexagonal perovskite derivatives containing palmierite-like layers [63, 66, 67]. Bond-valence site energy calculations similarly evidence three-dimensional connectivity across the different oxygen positions (Figure S14). The relative BVS energy barriers for O1–O2 and O2–O2 hopping (~ 0.30 and ~ 0.55 eV, respectively) are comparable with the barrier for O1–O1 hopping (~ 0.23 eV), and considerably lower than the analogous BVSE barriers for oxygen migration along the *c*-axis reported for $Ba_3M'M''O_{8.5}$ (*M*' = V, Nb, Ge; *M*" = Mo) hexagonal derivatives (> 0.70 and > 1.1 eV), [39, 68] thus demonstrating that these pathways can offer a sizeable contribution to the oxide ion diffusion in $A_3V_2O_8$ probably due to the ease of rotation of the polyhedral units.

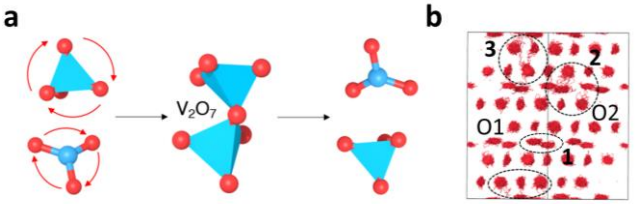

Figure 6. (a) Schematic of the oxygen migration mechanism via the formation of a V_2O_7 group via condensation of a VO_4 tetrahedron with an oxygen-deficient VO_3 group. Rotation of the polyhedral units facilitates the ionic transport. **(b)** AIMD trajectory plot for oxide ions in $Sr_3V_2O_8$ with an oxygen vacancy concentration of 6.25% at 1200 K. The circled areas evidence exchange between O1–O1 (**1**), O1–O2 (**2**) and O2–O2 (3) positions.

Conclusions

In summary, we reported significant proton and oxide ion conductivity in palmierite oxides $A_3V_2O_8$ (A = Sr, Ba). These systems present prevalent ionic conduction with a large protonic component under humidified air (t_H ~ 0.6 – 0.8). In particular, the proton conductivity of $Sr_3V_2O_8$ is competitive with other proton conductors constituted by isolated tetrahedral units. Protons incorporated in the $A_3V_2O_8$ structure have high mobility and our results suggest that the introduction of extrinsic oxygen vacancies by chemical acceptor doping can favor water absorption and further increase both the proton and oxide ion conductivity. Proton and oxide ion conduction through stabilization of oxygen vacancy defects in oxide-type structures constituted by isolated tetrahedral units is rare, with only examples constituted by scheelite-type oxides and doped $La_{1-x}Ba_{1+x}GaO_{4-x/2}$. [28, 31] Studies on hexagonal perovskite derivatives have evidenced that oxygen interstitial defects can also be stabilized within palmierite-like motifs resulting in increased ionic conductivity. [69] Palmierite oxides constitute a promising new family of ionic conductors where stabilization of parallel vacancy and interstitial defects can be employed for the design of materials with improved conductivities.

ASSOCIATED CONTENT

Supporting Information. The supporting information includes figures showing further electrochemical data; details of the equivalent circuit analysis; figures and tables of crystallographic data; figures and tables of further results of DFT, AIMD and BVSE calculations; thermogravimetric data.

AUTHOR INFORMATION

Corresponding Author

*** Sacha Fop**; orcid.org/0000-0003-4168-6363
Email: sacha.fop@stfc.ac.uk

Authors

James A. Dawson; orcid.org/0000-0002-3946-5337
Dylan N. Tawse
Matthew G. Skellern
Jan. M. S. Skakle; orcid.org/0000-0001-5249-5306
Abbie C. Mclaughlin; orcid.org/0000-0001-9960-723X

FUNDING SOURCES

This research was supported by the Leverhulme-Trust (RPG-2017-351 and RF-2020-295\4).

NOTES

The authors declare no competing financial interest.

ACKNOWLEDGMENT

We acknowledge the UK Science and Technology Facilities Council (STFC) for provision of neutron beamtime at ISIS. JAD gratefully acknowledges Newcastle University for funding through a Newcastle Academic Track (NUAcT) Fellowship. Via membership of the UK's HEC Materials Chemistry Consortium, which is funded by the EPSRC (EP/R029431), this work used the ARCHER2 UK National Supercomputing Service.

REFERENCES

[1] Steele, B. C.; Heinzel. A. Materials for Fuel-Cell Technologies. *Nature* **2001**, *414*, 345-352.

[2] Wachsman, E. D.; Lee, K. T. Lowering the Temperature of Solid Oxide Fuel Cells. *Science* **2011***, 334*, 935-939.

[3] Duan, C.; Tong, J.; Shang, M.; Nikodemski, S.; Sanders, M.; Ricote, S.; Almansoori, A.; O'Hayre, R. Readily Processed Protonic Ceramic Fuel Cells with High Performance at Low Temperatures. *Science* **2015***, 349*, 1321-1326.

[4] Choi, S.; Kucharczyk, C. J.; Liang, Y.; Zhang, X.; Takeuchi, I.; Ji, H.; Haile, S. M. Exceptional Power Density and Stability at Intermediate Temperatures in Protonic Ceramic Fuel Cells. *Nature Energy* **2018***, 3*, 202-210.

[5] Duan, C.; Kee, R.; Zhu, H.; Sullivan, N.; Zhu, L.; Bian, L.; Jennings, D.; O'Hayre, R. Highly Efficient Reversible Protonic Ceramic Electrochemical Cells for Power Generation and Fuel Production. *Nature Energy* **2019***, 4*, 230-240.

[6] Choi, S.; Davenport, T. C.; Haile, S. M. Protonic Ceramic Electrochemical Cells for Hydrogen Production and Electricity Generation: Exceptional Reversibility, Stability, and Demonstrated Faradaic Efficiency. *Energy Environ. Sci.* **2019***, 12*, 206-215.

[7] Mogensen, M. B.; Chen, M.; Frandsen, H. L.; Graves, C.; Hansen, J. B.; Hansen, K. V.; Hauch, A.; Jacobsen, T.; Jensen, S. H.; Skafte, T. L.; Sun, X. Reversible Solid-Oxide Cells for Clean and Sustainable Energy. *Clean En* **2019***, 3*, 175-201.

[8] Marnellos, G.; Stoukides, M. Ammonia Synthesis at Atmospheric Pressure. *Science* **1998***, 282*, 98.

[9] Morejudo, S. H.; Zanón, R.; Escolástico, S.; Yuste-Tirados, I.; Malerød-Fjeld, H.; Vestre, P. K.; Coors, W. G.; Martínez, A.; Norby, T.; Serra, J. M.; Kjølseth, C. Direct Conversion of Methane to Aromatics in a Catalytic Co-Ionic Membrane Reactor. *Science* **2016***, 353*, 563-566.

[10] Kreuer, K. D. Proton-Conducting Oxides. *Annu. Rev. Mater. Res*. **2003**, *33*, 333–359.

[11] Malavasi, L.; Fisher, C. A. J.; Islam, M. S. Oxide-Ion and Proton Conducting Electrolyte Materials for Clean Energy Applications: Structural and Mechanistic Features. *Chem. Soc. Rev.* **2010***, 39*, 4370-4387.

[12] Fabbri, E.; Pergolesi, D.; Traversa, E. Materials Challenges Toward Proton-Conducting Oxide Fuel Cells: A Critical Review. *Chem. Soc. Rev.* **2010***, 39*, 4355-4369.

[13] Ishihara, T.; Matsuda, H.; Takita, Y. Doped $LaGaO_3$ Perovskite Type Oxide as a New Oxide Ionic Conductor. *J. Am. Chem. Soc.* **1994***, 116*, 3801-3803.

[14] Li, M.; Pietrowski, M. J.; De Souza, R. A.; Zhang, H.; Reaney, I. M.; Cook, S. N.; Kilner, J. A.; Sinclair, D. C. A Family Of Oxide Ion Conductors Based on the Ferroelectric Perovskite $Na_{0.5}Bi_{0.5}TiO_3$. *Nat. Mater.* **2013***, 13*, 31-35.

[15] Islam, M. S. Ionic Transport in ABO_3 Perovskite Oxides: A Computer Modelling Tour. *J. Mater. Chem.* **2000***, 10*, 1027-1038.

[16] Zhang, H.; Ramadan, A. H. H.; De Souza, R. A. Atomistic Simulations of Ion Migration in Sodium Bismuth Titanate (NBT) Materials: Towards Superior Oxide-Ion Conductors. *J. Mater. Chem. A* **2018***, 6*, 9116-9123.

[17] Dawson, J. A.; Miller, J. A.; Tanaka, I. First-Principles Insight into the Hydration Ability and Proton Conduction of the Solid State Proton Conductor, Y and Sn Co-Doped $BaZrO_3$. *Chem. Mater.* **2015***, 27*, 901-908.

[18] Fop, S. Solid Oxide Proton Conductors Beyond Perovskites. *J. Mater. Chem. A* **2021***, 9*, 18836-18856.

[19] Fujii, K.; Esaki, Y.; Omoto, K.; Yashima, M.; Hoshikawa, A.; Ishigaki, T.; Hester, J. R. New Perovskite-Related Structure Family of Oxide-Ion Conducting Materials $NdBaInO_4$. *Chem. Mater.* **2014***, 26*, 2488-2491.

[20] Zhang, W.; Fujii, K.; Niwa, E.; Hagihala, M.; Kamiyama, T.; Yashima, M. Oxide-Ion Conduction in the Dion–Jacobson Phase $CsBi_2Ti_2NbO_{10-\delta}$. *Nature Communications* **2020***, 11*, 1224.

[21] Amezawa, K.; Tomii, Y.; Yamamoto, N. High Temperature Protonic Conduction in $LaPO_4$ Doped with Alkaline Earth Metals. *Solid State Ionics* **2005***, 176*, 135-141.

[22] Haugsrud, R.; Norby, T. Proton conduction in rare-earth orthoniobates and ortho-tantalates. *Nature Materials* **2006***, 5*, 193-196.

[23] Haugsrud, R.; Norby, T. High-Temperature Proton Conductivity in Acceptor-Substituted Rare-Earth Ortho-Tantalates, $LnTaO_4$. *J. Am. Ceram. Soc.* **2007***, 90*, 1116-1121.

[24] Huse, M.; Norby, T.; Haugsrud, R. Proton Conductivity in Acceptor-Doped $LaVO_4$. *J. Electrochem. Soc.* **2011***, 158*, B857.

[25] Bjørheim, T. S.; Norby, T.; Haugsrud, R. Hydration and Proton Conductivity in $LaAsO_4$. *J. Mater. Chem.* **2012***, 22*, 1652-1661.

[26] Winiarz, P.; Dzierzgowski, K.; Mielewczyk-Gryń, A.; Gazda, M.; Wachowski, S. High-Temperature Proton Conduction in $LaSbO_4$. *Chem. Eur. J.* **2021***, 27*, 5393-5398.

[27] Li, S.; Schönberger, F.; Slater, P. $La_{1-x}Ba_{1+x}GaO_{4-x/2}$: a Novel High Temperature Proton Conductor. *Chem. Commun.* **2003**, 2694-2695.

[28] Kendrick, E.; Kendrick, J.; Knight, K. S.; Islam, M. S.; Slater, P. R. Cooperative Mechanisms of Fast-Ion Conduction in Gallium-Based Oxides with Tetrahedral Moieties. *Nature Materials* **2007***, 6*, 871.

[29] Iakovleva, A.; Chesnaud, A.; Animitsa, I.; Dezanneau, G. Insight into the Synthesis and Electrical Properties of Alkali-Earth-Substituted Gd_3GaO_6 Oxide-Ion and Proton Conductors. *Int. J. Hydrogen Energy* **2016***, 41*, 14941-14951.

[30] Kendrick, E.; Islam, M. S.; Slater, P. R. Developing Apatites for Solid Oxide Fuel Cells: Insight Into Structural, Transport and Doping Properties. *J. Mater. Chem.* **2007***, 17*, 3104-3111.

[31] Yang, X.; Fernández-Carrión, A. J.; Wang, J.; Porcher, F.; Fayon, F.; Allix, M.; Kuang, X. Cooperative Mechanisms of Oxygen Vacancy Stabilization and Migration in the Isolated Tetrahedral Anion Scheelite Structure. *Nature Communications* **2018***, 9*, 4484.

[32] Auckett, J. E.; Lopez-Odriozola, L.; Clark, S. J.; Evans, I. R. Exploring the Nature of the Fergusonite–Scheelite Phase Transition and Ionic Conductivity Enhancement by Mo^{6+} Doping in $LaNbO_4$. *J. Mater. Chem. A* **2021***, 9*, 4091-4102.

[33] Fop, S.; Skakle, J. M. S.; McLaughlin, A. C.; Connor, P. A.; Irvine, J. T. S.; Smith, R. I.; Wildman, E. J. Oxide Ion Conductivity in the Hexagonal Perovskite Derivative $Ba_3MoNbO_{8.5}$. *J. Am. Chem. Soc.* **2016***, 138*, 16764-16769.

[34] Fop, S.; Wildman, E. J.; Irvine, J. T. S.; Connor, P. A.; Skakle, J. M. S.; Ritter, C.; Mclaughlin, A. C. Investigation of the Relationship between the Structure and Conductivity of the Novel Oxide Ionic Conductor $Ba_3MoNbO_{8.5}$. *Chem. Mater.* **2017***, 29*, 4146-4152.

[35] Fop, S.; Wildman, E. J.; Skakle, J. M. S.; Ritter, C.; Mclaughlin, A. C. Electrical and Structural Characterization of $Ba_3Mo_{1-x}Nb_{1+x}O_{8.5-x/2}$: The Relationship between Mixed Coordination, Polyhedral Distortion and the Ionic Conductivity of $Ba_3MoNbO_{8.5}$. *Inorg. Chem.* **2017***, 56*, 10505-10512.

[36] McCombie, K. S.; Wildman, E. J.; Fop, S.; Smith, R. I.; Skakle, J. S.; Mclaughlin, A. C. The Crystal Structure and Electrical Properties of the Oxide Ion Conductor $Ba_3WNbO_{8.5}$. *J. Mater. Chem. A* **2018***, 6*, 5290-5295.

[37] Fop, S.; McCombie, K. S.; Wildman, E. J.; Skakle, J. M. S.; Mclaughlin, A. C. Hexagonal Perovskite Derivatives: a New

Direction in the Design of Oxide Ion Conducting Materials. *Chem. Commun.* **2019***, 55*, 2127-2137.
[38] Gilane, A.; Fop, S.; Sher, F.; Smith, R. I.; Mclaughlin, A. C. The Relationship Between Oxide-Ion Conductivity and Cation Vacancy Order in the Hybrid Hexagonal Perovskite $Ba_3VWO_{8.5}$. *J. Mater. Chem. A* **2020***, 8*, 16506-16514.
[39] Fop, S.; McCombie, K.; Smith, R. I.; Mclaughlin, A. C. Enhanced Oxygen Ion Conductivity and Mechanistic Understanding in $Ba_3Nb_{1-x}V_xMoO_{8.5}$. *Chem. Mater.* **2020***, 32*, 4724-4733.
[40] Fop, S.; McCombie, K. S.; Wildman, E. J.; Skakle, J. M. S.; Irvine, J. T. S.; Connor, P. A.; Savaniu, C.; Ritter, C.; Mclaughlin, A. C. High Oxide Ion and Proton Conductivity in a Disordered Hexagonal Perovskite. *Nature Materials* **2020***, 19*, 752-757.
[41] Darriet, J.; Subramanian, M. A. Structural Relationships Between Compounds Based on the Stacking of Mixed Layers Related to Hexagonal Perovskite-Type Structures. *J. Mater. Chem.* **1995***, 5*, 543-552.
[42] Skakle, J. M. S.; Coats, A. M.; Marr, J. The Crystal Structures of $Ba_2R_{2/3}V_2O_8$ (R = La, Nd) and $Sr_2La_{2/3}V_2O_8$; Palmierite Derivatives. *J. Mater. Sci.* **2000***, 35*, 3251-3256.
[43] Toby, B. H. EXPGUI a Graphical User Interface for GSAS. *Journal of Applied Crystallography* **2001***, 34*, 210-213.
[44] Chen, H.; Wong, L. L.; Adams, S. SoftBV - a Software Tool for Screening the Materials Genome of Inorganic Fast Ion Conductors. *Acta Crystallographica Section B* **2019***, 75*, 18-33.
[45] Wong, L. L.; Phuah, K. C.; Dai, R.; Chen, H.; Chew, W. S.; Adams, S. Bond Valence Pathway Analyzer—An Automatic Rapid Screening Tool for Fast Ion Conductors within softBV. *Chem. Mater.* **2021***, 33*, 625-641.
[46] Blöchl, P. E. Projector Augmented-Wave Method. *Phys. Rev. B: Condens. Matter Mater. Phys*. **1994**, *50*, 17953−17979.
[47] Perdew, J. P.; Ruzsinszky, A.; Csonka, G. I.; Vydrov, O. A.; Scuseria, G. E.; Constantin, L. A.; Zhou, X.; Burke, K. Restoring the Density-Gradient Expansion for Exchange in Solids and Surfaces. *Phys. Rev. Lett*. **2008**, *100*, 136406.
[48] D.J. Evans, B.L. Holian, The Nose–Hoover Thermostat, *J. Chem. Phys*. **1985**, *83*, 4069–4074.
[49] Irvine, J. T. S.; Sinclair, D. C.; West, A. R. Electroceramics: Characterization by Impedance Spectroscopy. *Adv. Mater.* **1990***, 2*, 132-138.
[50] Bonanos, N.; Huijser, A.; Poulsen, F. W. H/D Isotope Effects in High Temperature Proton Conductors. *Solid State Ionics* **2015***, 275*, 9-13.
[51] Zhang, G. B.; Smyth, D. M. Protonic Conduction in $Ba_2In_2O_5$. *Solid State Ionics* **1995***, 82*, 153-160.
[52] Verbraeken, M. C.; Cheung, C.; Suard, E.; Irvine, J. T. S. High H^- ionic conductivity in barium hydride. *Nature Materials* **2014***, 14*, 95.
[53] Fuller, C. A.; Blom, D. A.; Vogt, T.; Evans, I. R.; Evans, J. S. O. Oxide Ion and Proton Conductivity in a Family of Highly Oxygen-Deficient Perovskite Derivatives. *J. Am. Chem. Soc.* **2022***, 144*, 615-624.
[54] Bjørheim, T. S.; Haugsrud, R. Proton Transport Properties of the $RE_3Ga_5MO_{14}$ (RE=La, Nd and M=Si, Ti, Sn) Langasite Family of Oxides. *Solid State Ionics* **2015***, 275*, 29-34.
[55] Martín-Sedeño, M. C.; Marrero-López, D.; Losilla, E. R.; León-Reina, L.; Bruque, S.; Núñez, P.; Aranda, M. A. G. Structural and Electrical Investigation of Oxide Ion and Proton Conducting Titanium Cuspidines. *Chem. Mater.* **2005***, 17*, 5989-5998.
[56] Auckett, J. E.; Milton, K. L.; Evans, I. R. Cation Distributions and Anion Disorder in $Ba_3NbMO_{8.5}$ (M = Mo, W) Materials: Implications for Oxide Ion Conductivity. *Chem. Mater.* **2019***, 31*, 1715-1719.
[57] Chambers, M. S.; McCombie, K. S.; Auckett, J. E.; McLaughlin, A. C.; Irvine, J. T. S.; Chater, P. A.; Evans, J. S. O.; Evans, I. R. Hexagonal Perovskite Related Oxide Ion Conductor $Ba_3NbMoO_{8.5}$: Phase Transition, Temperature Evolution of the Local Structure and Properties. *J. Mater. Chem. A* **2019***, 7*, 25503-25510.
[58] Wildman, E. J.; Mclaughlin, A. C.; Macdonald, J. F.; Hanna, J. V.; Skakle, J. M. S. The Crystal Structure of $Ba_3Nb_2O_8$ Revisited: A Neutron Diffraction and Solid-State NMR Study. *Inorg. Chem.* **2017***, 56*, 2653-2661.
[59] S. Fop, *ISIS Neutron and Muon source*, 2021, (DOI:10.5286/ISIS.E.RB2190080).
[60] Mather, G. C.; Heras-Juaristi, G.; Ritter, C.; Fuentes, R. O.; Chinelatto, A. L.; Pérez-Coll, D.; Amador, U. Phase Transitions, Chemical Expansion, and Deuteron Sites in the $BaZr_{0.7}Ce_{0.2}Y_{0.1}O_{3-\delta}$ Proton Conductor. *Chem. Mater.* **2016***, 28*, 4292-4299.
[61] Kendrick, E.; Knight, K. S.; Islam, M. S.; Slater, P. R. Structural Studies of the Proton Conducting Perovskite '$La_{0.6}Ba_{0.4}ScO_{2.8}$'. *Solid State Ionics* **2007***, 178*, 943-949.
[62] Münch, W.; Kreuer, K. -.; Seifert, G.; Maier, J. Proton Diffusion in Perovskites: Comparison Between $BaCeO_3$, $BaZrO_3$, $SrTiO_3$, and $CaTiO_3$ Using Quantum Molecular Dynamics. *Solid State Ionics* **2000***, 136-137*, 183-189.
[63] Fop, S.; Dawson, J. A.; Fortes, A. D.; Ritter, C.; McLaughlin, A. C. Hydration and Ionic Conduction Mechanisms of Hexagonal Perovskite Derivatives. *Chem. Mater.* **2021***, 33*, 4651-4660.
[64] Gilane, A.; Fop, S.; Tawse, D. N.; Ritter, C.; Mclaughlin, A. C. Variable Temperature Neutron Diffraction Study of the Oxide Ion Conductor $Ba_3VWO_{8.5}$. *Inorg. Chem.* **2022**, *61*, 1597-1602.
[65] Kim, G.; Griffin, J. M.; Blanc, F.; Haile, S. M.; Grey, C. P. Characterization of the Dynamics in the Protonic Conductor CsH_2PO_4 by ^{17}O Solid-State NMR Spectroscopy and First-Principles Calculations: Correlating Phosphate and Protonic Motion. *J. Am. Chem. Soc.* **2015***, 137*, 3867-3876.
[66] Yashima, M.; Tsujiguchi, T.; Fujii, K.; Niwa, E.; Nishioka, S.; Hester, J. R.; Maeda, K. Direct Evidence For Two-Dimensional Oxide-Ion Diffusion in the Hexagonal Perovskite-Related Oxide $Ba_3MoNbO_{8.5-\delta}$. *J. Mater. Chem. A* **2019***, 7*, 13910-13916.
[67] Yashima, M.; Tsujiguchi, T.; Sakuda, Y.; Yasui, Y.; Zhou, Y.; Fujii, K.; Torii, S.; Kamiyama, T.; Skinner, S. J. High Oxide-Ion Conductivity Through the Interstitial Oxygen Site In $Ba_7Nb_4MoO_{20}$-Based Hexagonal Perovskite Related Oxides. *Nature Communications* **2021***, 12*, 556.
[68] Cheng, Z.; Yang, J.; Jiang, P.; Huang, H.; da-Silva, I.; Gao, W.; Cong, R.; Yang, T. Enhancing the Oxide-Ionic Conductivity of $Ba_3Mo_{1+x}Nb_{1-2x}Ge_xO_{8.5}$ at Intermediate Temperatures: the Effect of Site-Selective Ge_{4+}-substitution. *Dalton Trans.* **2021***, 50*, 17249-17256.
[69] Yashima, M.; Tsujiguchi, T.; Sakuda, Y.; Yasui, Y.; Zhou, Y.; Fujii, K.; Torii, S.; Kamiyama, T.; Skinner, S. J. High oxide-ion conductivity through the interstitial oxygen site in $Ba_7Nb_4MoO_{20}$-based hexagonal perovskite related oxides. *Nature Communications* **2021***, 12*, 556.

Supplementary information for

Proton and Oxide Ion Conductivity in Palmierite Oxides

Sacha Fop,[1,2,*] James A. Dawson,[3,4] Dylan N. Tawse,[2] Matthew G. Skellern,[2] Jan M. S. Skakle,[2] and Abbie C. Mclaughlin[2]

[1] ISIS Facility, Rutherford Appleton Laboratory, Harwell OX11 0QX, United Kingdom
[2] The Chemistry Department, University of Aberdeen, Aberdeen AB24 3UE, United Kingdom
[3] Chemistry – School of Natural and Environmental Science, Newcastle University, Newcastle NE1 7RU, United Kingdom
[4] Centre for Energy, Newcastle University, Newcastle NE1 7RU, United Kingdom

* sacha.fop@stfc.ac.uk

Table S1. Lattice parameters for the computed structures at 0 K. The calculated unit cell parameters are in good agreement with the experimental values (see Tables S2 and S3).

	a **(Å)**	***c*** **(Å)**
$Sr_3V_2O_8$	5.590	20.079
$Sr_3V_2O_8 \cdot 0.0825H_2O$	5.621	20.060
$Sr_3V_2O_8 \cdot 0.330\ H_2O$	5.651	20.059
$Ba_3V_2O_8$	5.762	21.357
$Ba_3V_2O_8 \cdot 0.0825H_2O$	5.777	21.355
$Ba_3V_2O_8 \cdot 0.330H_2O$	5.843	21.303

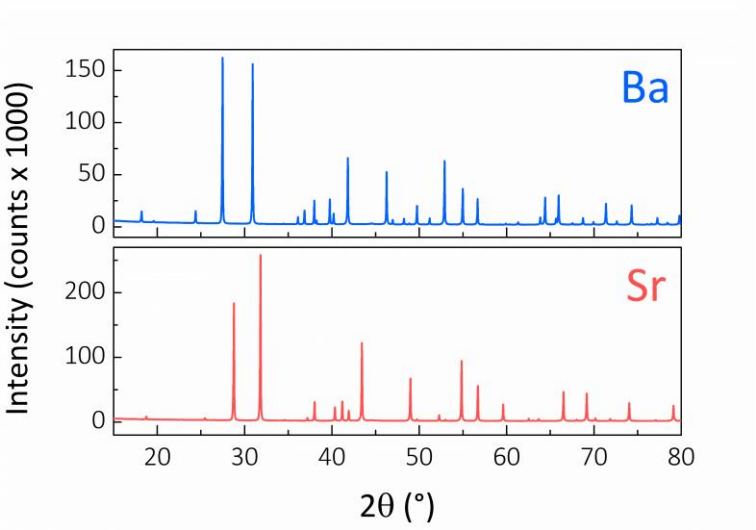

Figure S1. Laboratory X-ray diffraction patterns of as prepared $A_3V_2O_8$ (A = Sr, Ba).

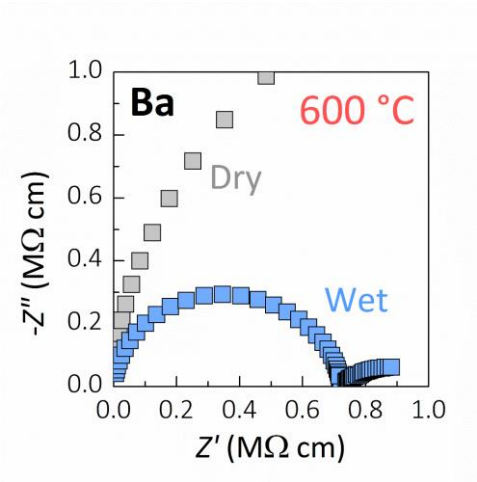

Figure S2. Complex impedance plot of $Ba_3V_2O_8$ collected under dry and wet air at 600 °C. The data show a clear reduction in resistivity on going from dry to humidified air. The complex impedance plot collected under wet air presents a Warburg response at low frequencies.

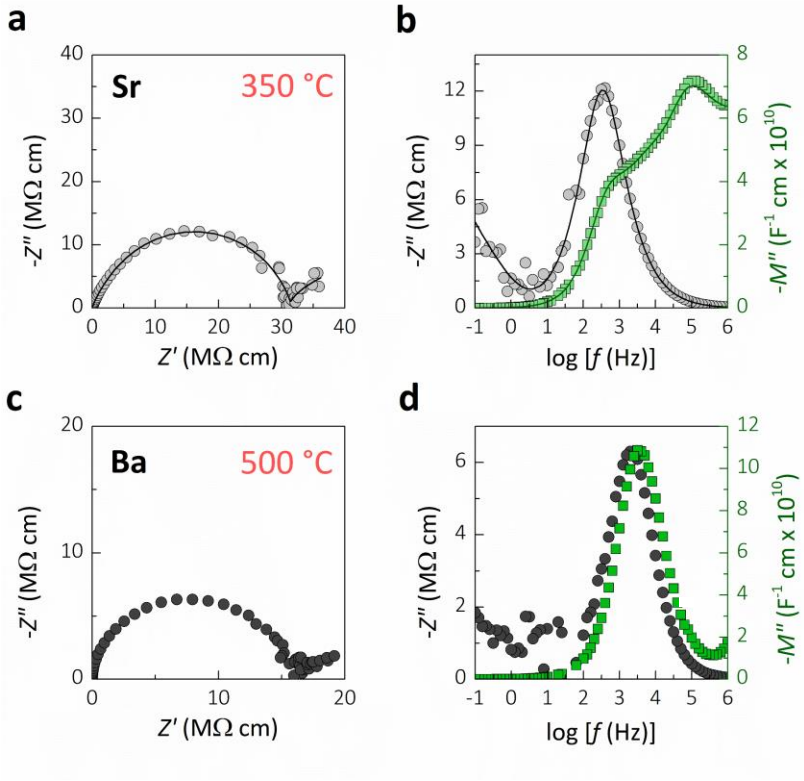

Figure S3. Complex impedance plot **(a)** and complex modulus (*M*") and impedance (*Z*") spectroscopic (Bode) plots **(b)** of $Sr_3V_2O_8$ collected under dry air at 350 °C. The complex modulus plot shows two peaks, one associated to the bulk response (high frequency) and the other associated to the grain boundary response (intermediate frequency). The most resistive part of the sample (grain boundary) is highlighted by the *Z*" spectroscopic plot, while the modulus plot highlights the element with the smallest capacitance (bulk) [1]. The lines represent the equivalent circuit fitting to the data. Complex impedance plot **(c)** and Bode plots **(d)** of $Ba_3V_2O_8$ collected under dry air at 500 °C. The complex modulus and impedance spectroscopic plots show a single peak which is associated to the overall grain response.

2. Equivalent circuit analysis

An equivalent circuit (EC) fitting procedure was employed to extract the individual bulk, grain boundary and electrode responses for the impedance data of $Sr_3V_2O_8$ collected under dry and humidified air atmosphere. The following equivalent circuit was used to model the impedance data,

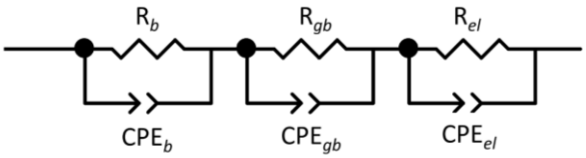

where R indicates a resistor, CPE a constant phase element; the subscript *b* stands for bulk, *gb* for grain boundary and *el* for electrode.

The complex impedance data of $Sr_3V_2O_8$ are composed by overlapping bulk and grain boundary arcs, together with a pronounced Warburg signal in the low frequency region. Equivalent circuit fits at selected temperatures are presented in Figure S4. The good match between the observed and calculated spectra is evident from the graphs.

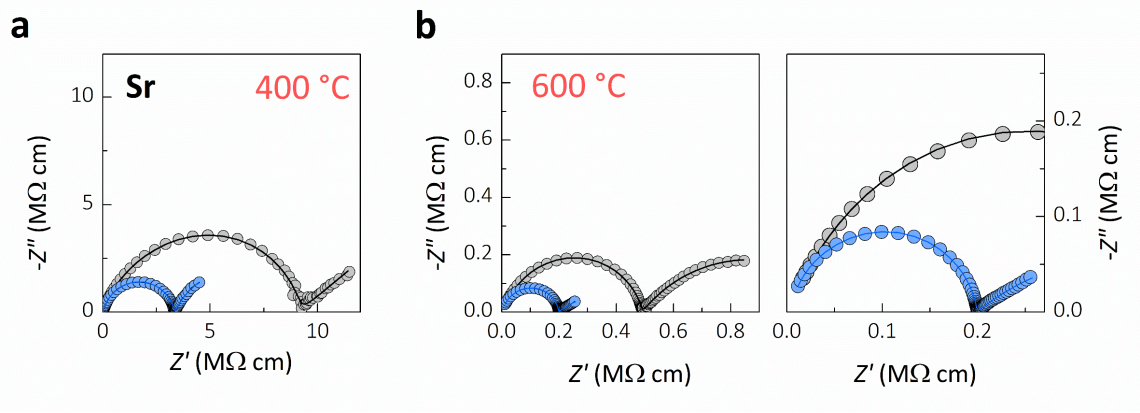

Figure S4. Complex impedance plots of $Sr_3V_2O_8$ recorded under dry (grey symbols) and humidified (blue symbols) air at 400 °C **(a)** and 600 °C **(b)**. The lines represent the equivalent circuit fitting. The right panel in **(b)** is a magnification of the wet air data.

The validity of the equivalent circuit analysis can be further evaluated by inspection of the distribution of the EC residuals ($\Delta Z'_{EC}$, $\Delta Z''_{EC}$) versus the logarithm of the frequency. The residuals from the equivalent circuit analysis present small values, with a variation generally smaller than 2% for the dry air data and smaller than 0.5% in the case of the data collected under humidified air (Figure S4). The values are also reasonably scattered along log(*f*), further validating the quality of the employed model [2].

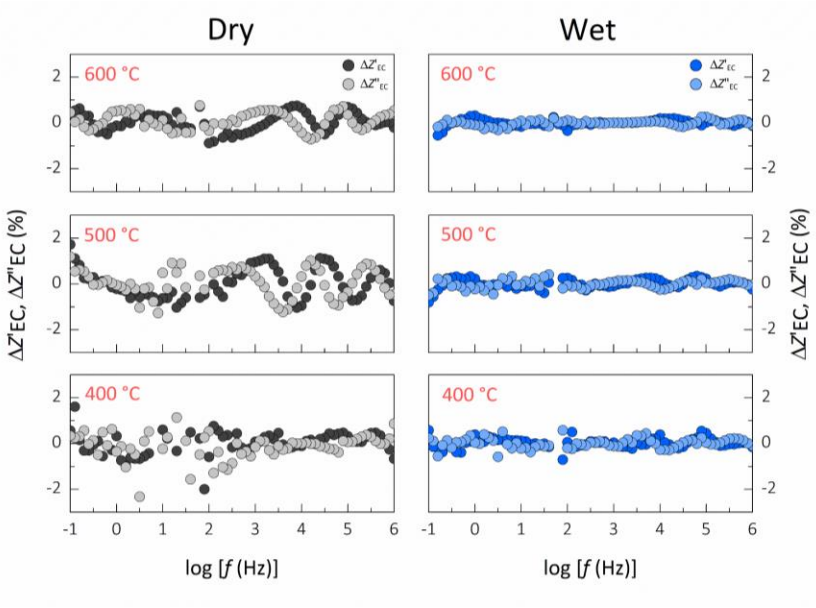

Figure S5. Typical residual plots of the equivalent circuit fitting procedure for the impedance data of $Sr_3V_2O_8$ at selected temperatures. The good match between observed and calculated impedance data, and the generally random distribution of the residuals indicate that the employed equivalent circuit model adequately represents the collected data.

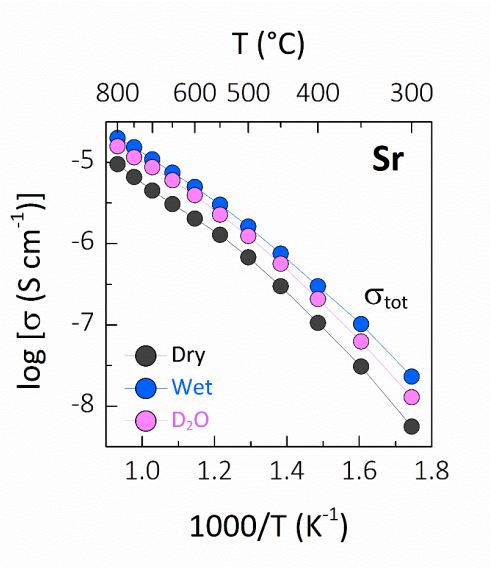

Figure S6. Arrhenius plot showing a reduction of the total conductivity of $Sr_3V_2O_8$ under air + D_2O atmosphere due to the isotope effect.

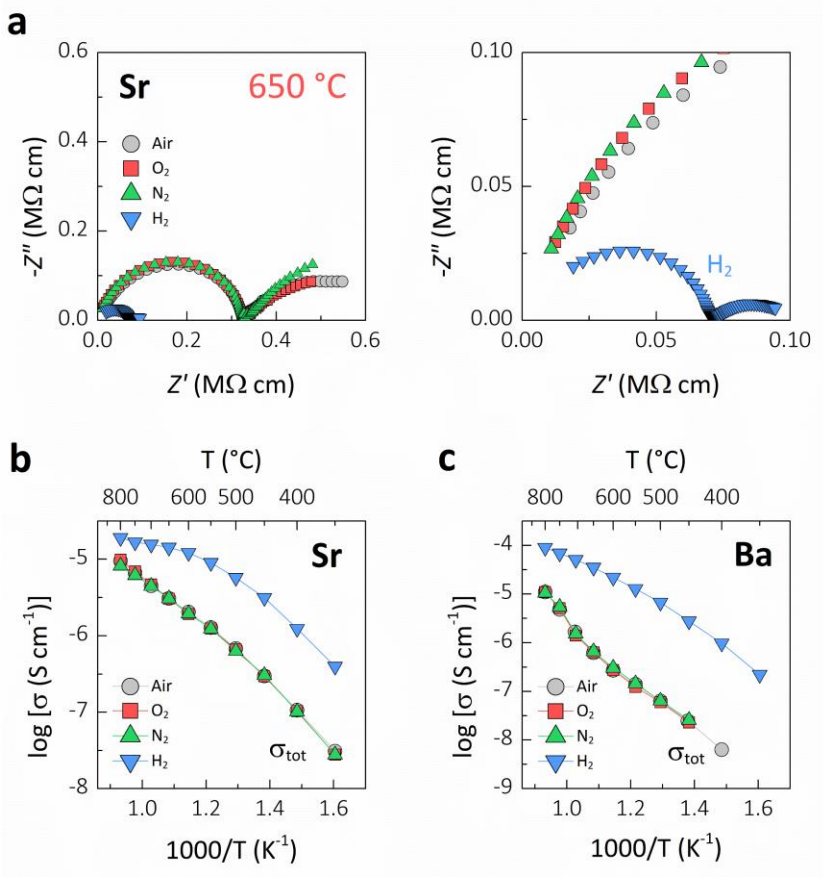

Figure S7. (a) Complex impedance plots of $Sr_3V_2O_8$ recorded under dry atmospheres (air, O_2, N_2 and 5% H_2 in N_2) at 650 °C. The right panel shows a magnification of the data collected under dry hydrogen atmosphere. The sample response is independent of the atmosphere at high-intermediate partial pressure of oxygen. The behaviour of the low-frequency electrode signal is consistent with oxygen ion conduction and Warburg diffusion [1]. **(b)**, **(c)** Arrhenius plots of the total conductivities of $Sr_3V_2O_8$ and $Ba_3V_2O_8$ under dry atmospheres. The total conductivity does not depend on the oxygen partial pressure at high and intermediate pO_2 values, demonstrating that the $A_3V_2O_8$ samples present predominantly ionic (oxide ion) conductivity under dry atmospheres. There is an increase in the conductivity in 5% H_2 in N_2 (which is particularly pronounced for $Ba_3V_2O_8$) revealing an electronic *n*-type component under the more reducing conditions.

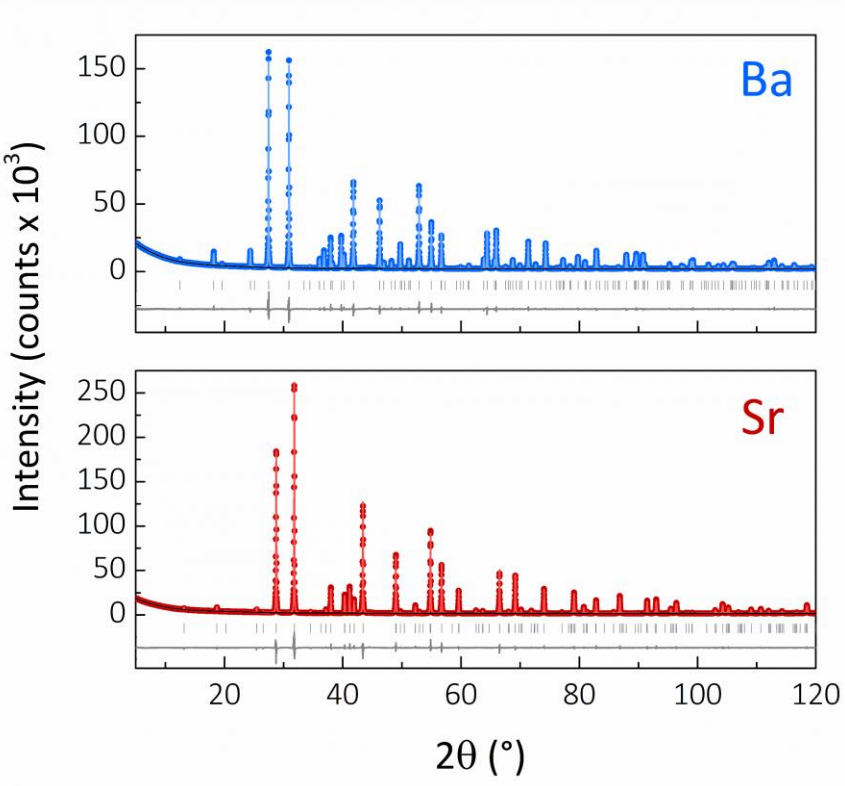

Figure S8. Rietveld histograms for the X-ray diffraction data of $A_3V_2O_8$ (A = Sr, Ba).

Table S2. Refined atomic parameters from Rietveld fit of the high-resolution X-ray diffraction data of $A_3V_2O_8$ (A = Sr, Ba) collected at room temperature (25 °C). Data were refined in the space group $R\bar{3}m$. The fractional occupancies of the different atoms refined within ± 1% of the full occupancy and were fixed to 1. All atoms were refined with isotropic displacement parameters, U_{iso} (Å^2).

			Sr	Ba
	***a* (Å)**		5.61801(2)	5.78366(2)
	***c* (Å)**		20.10050(9)	21.32148(9)
	***V* (Å^3)**		549.420(5)	617.667(5)
			Sr	**Ba**
A1	**3*a* (0,0,0)**	U_{iso}	0.0098(3)	0.0118(2)
A2	**6*c* (0,0,*z*)**	***z***	0.202071(4)	0.205288(2)
		U_{iso}	0.0015(5)	0.0009(1)
V1	**6*c* (0,0,*z*)**	***z***	0.4059(2)	0.40699(9)
		U_{iso}	0.0025(5)	0.0014(2)
O1	**6*c* (0,0,*z*)**	***z***	0.3230(1)	0.3315(6)
		U_{iso}	0.0288(5)	0.0455(6)
O2	**18*h* (*x*,$\bar{x}$,*z*)**	***x***	0.1698(2)	0.1541(7)
		z	0.5666(3)	0.5661(5)
		U_{iso}	0.0189(6)	0.0191(3)
			Sr	**Ba**
	χ^2		6.34	5.09
	Rp (%)		4.26	3.42
	Rwp (%)		6.63	5.27

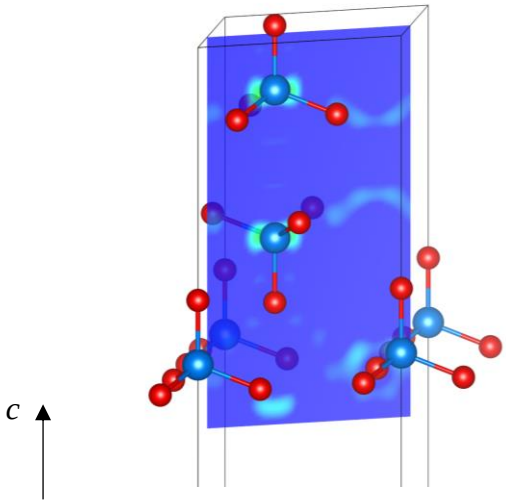

Figure S9. Section of X-ray difference Fourier map for $Sr_3V_2O_8$ as seen along the [100] direction at a y ~ 0.333. The metal V cations are represented by blue spheres, while the oxygen atoms are in red. The Ba atoms are omitted for clarity. Examination of X-ray difference Fourier maps shows no evidence of significant missing electron scattering density between the two V positions, indicating that the site is empty and the cation vacancies are fully ordered.

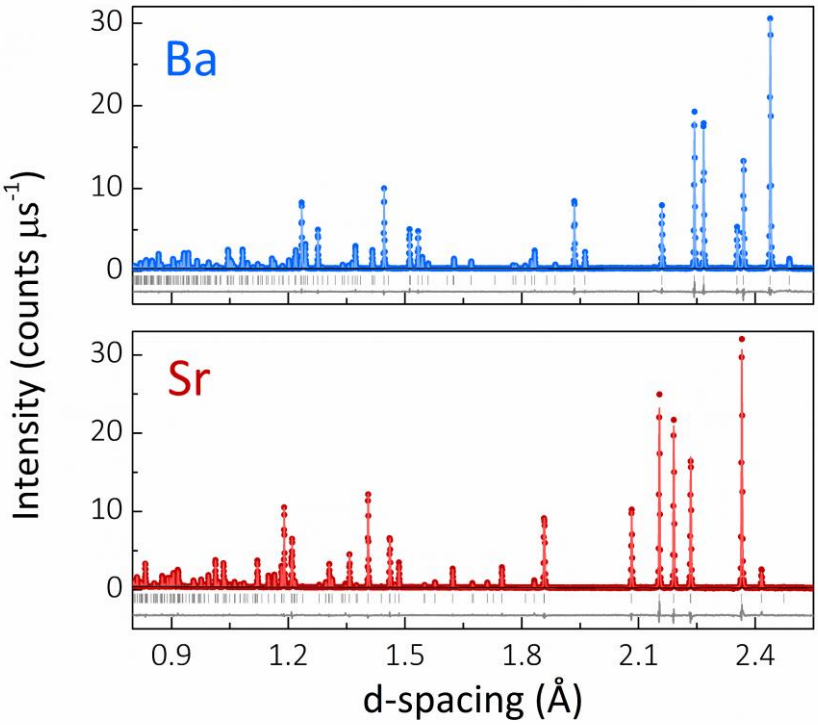

Figure S10. Rietveld histograms for the neutron diffraction data of $A_3V_2O_8$ (A = Sr, Ba) collected on HRPD. The TOF neutron diffraction data for the high-resolution backscattering detector of HRPD is shown.

Table S3. Refined atomic parameters from Rietveld fit of the high-resolution neutron diffraction data of $A_3V_2O_8$ (A = Sr, Ba) collected at room temperature (25 °C). Data were refined in the space group $R\bar{3}m$. The fractional occupancies of Ba and O refined within ± 1% of the full occupancy and were fixed to 1. The fractional occupancies of V were fixed to 1 from the results of the refinements of the structure from X-ray diffraction. The U_{13}, U_{23} anisotropic displacement parameters are zero for A1, A2, V1 and O1 due to the symmetry of the unit cell.

			Sr	Ba
	***a* (Å)**		5.61913(1)	5.784345(9)
	***c* (Å)**		20.10422(7)	21.32742(5)
	***V* (Å^3)**		549.740(2)	617.984(2)
			Sr	**Ba**
A1	**3*a* (0,0,0)**	$U_{11} = U_{22}$	0.0092(4)	0.0159(4)
		U_{33}	0.0053(5)	0.0071(5)
		U_{12}	0.0046(2)	0.0080(2)
A2	**6*c* (0,0,*z*)**	*z*	0.201981(8)	0.205054(3)
		$U_{11} = U_{22}$	0.0100(3)	0.0107(3)
		U_{33}	0.0016(4)	0.0092(4)
		U_{12}	0.0050(1)	0.0054(1)
V1	**6*c* (0,0,*z*)**	*z*	0.4070(4)	0.4063(4)
		$U_{11} = U_{22}$	0.0132(3)	0.0068(1)
		U_{33}	0.0135(2)	0.0072(1)
		U_{12}	0.0066(2)	0.0034(2)
O1	**6*c* (0,0,*z*)**	*z*	0.32244(3)	0.327876(2)
		$U_{11} = U_{22}$	0.0315(4)	0.0331(3)
		U_{33}	0.0050(3)	0.0079(4)
		U_{12}	0.0157(2)	0.0166(1)
O2	**18*h* (*x*,$\bar{x}$,*z*)**	*x*	0.16762(5)	0.16144(5)
		z	0.56528(3)	0.565546(1)
		U_{11}	0.0242(2)	0.0167(2)
		U_{22}	0.0040(3)	0.0167(2)
		U_{33}	0.0082(3)	0.0164(3)
		U_{12}	0.0020(1)	0.0120(2)
		U_{13}	0.0010(1)	0.0006(1)
		U_{23}	-0.0010(1)	-0.0006(1)
			Sr	**Ba**
	χ^2		4.21	2.35
	Rp (%)		4.70	3.60
	Rwp (%)		4.78	3.16

Table S4. Selected bond lengths and angles for $A_3V_2O_8$ (A = Sr, Ba).

	Sr	Ba
A1–O1 (Å)	3.25179(7)	3.34162(2)
A1–O2 (Å)	2.6096(7)	2.7599(4)
A2–O1 (Å)	2.4192(13)	2.6195(7)
A2–O2 (Å)	2.8736(2)	2.9501(1)
	2.5972(8)	2.8070(7)
V1–O1 (Å)	1.703(1)	1.673(8)
V1–O2 (Å)	1.708(5)	1.725(3)
O1–V1–O2 (°)	109.0(4)	110.4(2)
O2–V1–O2 (°)	109.9(2)	108.6(2)

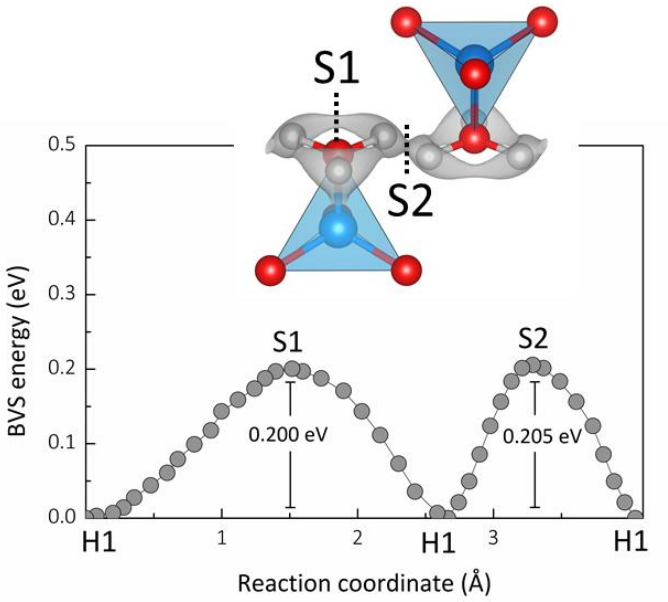

Figure S11. Connectivity between BVSE isosurfaces reveals a lowest energy 2-dimensional proton conduction pathway (isosurface levels at < 0.3 eV) composed by H1–H1 exchange and hopping onto adjacent oxygen atoms. BVSE model of proton migration barriers for proton exchange (S1) and hopping (S2) for $Sr_3V_2O_8$.

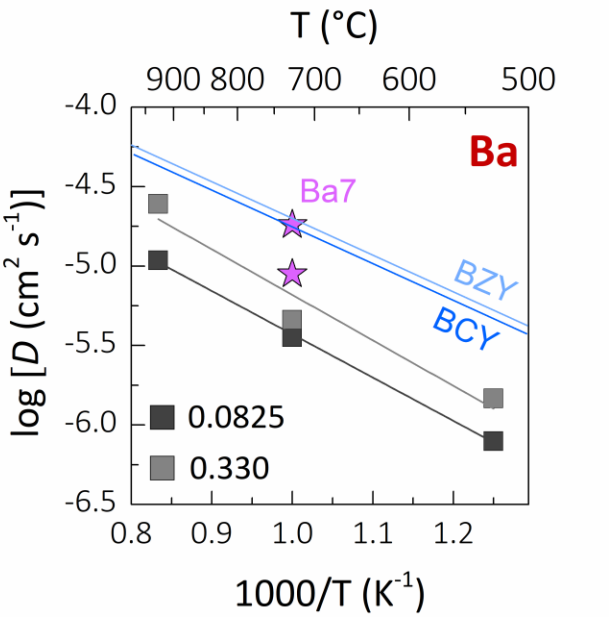

Figure S12. Arrhenius plot of the calculated proton diffusion coefficient for $Ba_3V_2O_8{\cdot}nH_2O$, with *n* = 0.0825 and 0.330. The diffusion coefficients for perovskite-type proton conductors $BaCe_{0.98}Y_{0.02}O_{3-\delta}$ (BCY) and $BaZr_{0.9}Y_{0.2}O_{3-\delta}$ (BZY) [3] and for $Ba_7Nb_4MoO_{20}{\cdot}nH_2O$ with n = 0.125 and 0.5 (Ba7) [4] are also plotted for comparison.

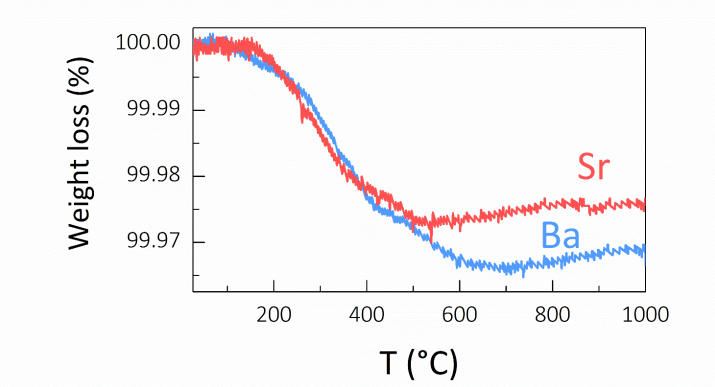

Figure S13. Results of thermogravimetric analysis on $A_3V_2O_8{\cdot}nH_2O$ (A = Sr, Ba) samples stored at ambient conditions. The weight losses correspond to water concentration of n = 0.008 for A = Sr and n = 0.013 for Ba.

Table S5. Hydration enthalpies of $A_3V_2O_8{\cdot}nH_2O$ (A = Sr, Ba) obtained by DFT calculations for different water uptakes (*n*). Hydration enthalpies were calculated based on the energy differences between the hydrated and dehydrated materials. For the materials with the lower water content ($0.0825H_2O$), we also considered the possibility of water molecules absorbing at pre-existing oxygen vacancy sites by comparing the energetics of the materials with an oxygen vacancy with those of the hydrated phases.

A	nH_2O		Hydration enthalpy (kJ mol^{-1})
Sr	0.0825		+10.61
	0.330		+87.80
	0.0825	Oxygen vacancy site	-63.00
Ba	0.0825		+68.51
	0.330		+77.19
	0.0825	Oxygen vacancy site	-32.81

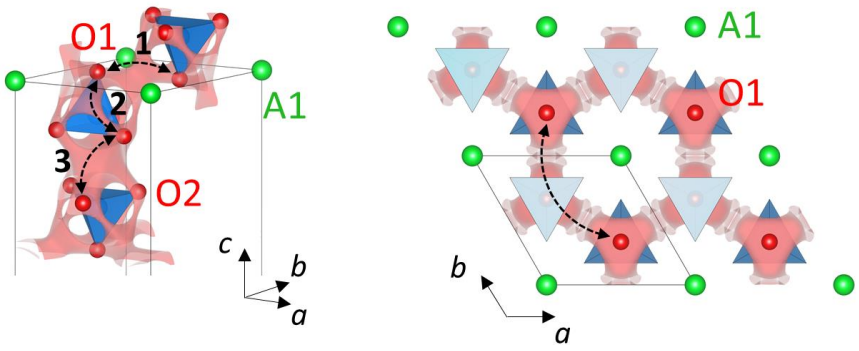

Figure S14. BVSE map for a test O^{2-} ion in $Sr_3V_2O_8$ showing three-dimensional connectivity suggesting exchange between O1–O1 (**1**), O1–O2 (**2**) and O2–O2 (**3**) positions. The panel on the left shows the BVSE path at z = 0 as seen along the [001] direction evidencing a curved trajectory around the A1 cations. Isosurfaces levels are drawn at < 0.6 eV.

References

[1] Irvine, J. T. S., Sinclair, D. C. & West, A. R. Electroceramics: Characterization by Impedance Spectroscopy. *Adv Mater* **2**, 132-138 (1990).

[2] Boukamp, B. A. Electrochemical Impedance Spectroscopy in Solid State Ionics: Recent Advances. *Solid State Ionics* **169**, 65-73 (2004).

[3] Münch, W.; Kreuer, K. -.; Seifert, G.; Maier, J. Proton Diffusion in Perovskites: Comparison Between $BaCeO_3$, $BaZrO_3$, $SrTiO_3$, and $CaTiO_3$ Using Quantum Molecular Dynamics. *Solid State Ionics* **2000***, 136-137*, 183-189.

[4] Fop, S.; Dawson, J. A.; Fortes, A. D.; Ritter, C.; McLaughlin, A. C. Hydration and Ionic Conduction Mechanisms of Hexagonal Perovskite Derivatives. *Chem. Mater.* **2021***, 33*, 4651-4660.